

## Impact of land use change on the urban-rural temperature disparity in Eastern China

Yanyu Wang<sup>a,b,c</sup>, Jun Wang<sup>b,\*</sup>, Huanxin Zhang<sup>b</sup>, Nathan Janecek<sup>b</sup>, Yi Wang<sup>d</sup>, Meng Zhou<sup>b</sup>, Pengke Shen<sup>e</sup>, Jianguo Tan<sup>f</sup>, Qianshan He<sup>g,h</sup>, Tiantao Cheng<sup>c,i,j,\*\*</sup>, Cheng Huang<sup>a,\*\*\*</sup>

<sup>a</sup> State Environmental Protection Key Laboratory of Formation and Prevention of Urban Air Pollution Complex, Shanghai Academy of Environmental Sciences, Shanghai, China

<sup>b</sup> Department of Chemical and Biochemical Engineering, Center for Global and Regional Environmental Research, Iowa Technology Institute, University of Iowa, Iowa City, IA, United States

<sup>c</sup> Department of Atmospheric and Oceanic Sciences, Institute of Atmospheric Sciences, Fudan University, Shanghai, China

<sup>d</sup> Key Laboratory of Regional Ecology and Environmental Change, School of Geography and Information Engineering, China University of Geosciences, Wuhan, China

<sup>e</sup> National Climate Center, China Meteorological Administration, Beijing, China

<sup>f</sup> Shanghai Meteorological IT Support Center, Shanghai, China

<sup>g</sup> Shanghai Meteorological Service, Shanghai, China

<sup>h</sup> Shanghai Key Laboratory of Meteorology and Health, Shanghai, China

<sup>i</sup> Innovation Center of Ocean and Atmosphere System, Zhuhai Fudan Innovation Research Institute, Zhuhai, China

<sup>j</sup> CMA-FDU Joint Laboratory of Marine Meteorology, Shanghai, China

### HIGHLIGHTS

- WRF model with satellite-based land parameters is developed to quantify the impact of land use change on temperature.
- New urban areas become warmer and less green, vegetation restoration occurs in old urban areas due to urban renewal.
- A much larger greenspace fraction and albedo management are suggested in urban areas to alleviate urban warming.

### ARTICLE INFO

#### Keywords:

Urban warming  
Vegetation degradation  
Land use and land cover change  
Atmospheric modeling

### ABSTRACT

Unprecedented land use and land cover change (LULCC) has occurred across China over the past two decades. While urban heat island effects have been well documented, few studies identified the LULCC-induced temperature disparity within cities and nearby rural areas. Through an integrated analysis of satellite observations and regional model simulations, this study quantifies LULCC effect on summer temperature in old urban areas (existed in 2003), new urban areas (developed after 2003) and rural areas (non-urban areas) over Eastern China in 2003–2019. The results show that LULCC causes urban areas to become warmer, with the effect being more pronounced in new urban areas than in old urban areas. Air temperature (2 m,  $T_2$ ) and surface temperature ( $TSK$ ) in new urban areas increase respectively by 1.69 °C and 3.40 °C, while in old urban areas,  $T_2$  ( $TSK$ ) increases by 0.10 °C (0.13 °C). Significant vegetation degradation is observed in new urban areas, whereas vegetation restoration occurs in old urban areas in recent years as a result of urban renewal. In contrast, LULCC cools and greens rural areas, with a 0.02 °C (0.03 °C) decrease in  $T_2$  ( $TSK$ ). Urbanization warming can spread to the suburbs, along with vegetation degradation. The analysis of surface energy budget reveals that the reduction in latent heat plays a dominant role in urban warming. Our study underscores that a much larger greenspace fraction and albedo management in urban areas are suggested as an inherent part of future LULCC policy to alleviate urban-rural temperature disparity.

\* Corresponding author.

\*\* Corresponding author. Department of Atmospheric and Oceanic Sciences, Institute of Atmospheric Sciences, Fudan University, Shanghai, China.

\*\*\* Corresponding author.

E-mail addresses: [jun-wang-1@uiowa.edu](mailto:jun-wang-1@uiowa.edu) (J. Wang), [ttcheng@fudan.edu.cn](mailto:ttcheng@fudan.edu.cn) (T. Cheng), [huangc@saes.sh.cn](mailto:huangc@saes.sh.cn) (C. Huang).

<https://doi.org/10.1016/j.atmosenv.2023.119850>

Received 27 November 2022; Received in revised form 14 April 2023; Accepted 14 May 2023

Available online 15 May 2023

1352-2310/© 2023 Elsevier Ltd. All rights reserved.

## 1. Introduction

Global mean surface temperature has increased dramatically since the 1980s (Parry et al., 2007). In addition to greenhouse gases and anthropogenic aerosols, land use and land cover change (LULCC) can substantially influence temperature and surface energy budget by altering the surface albedo, roughness, and evapotranspiration (Zhou et al., 2004; Peng et al., 2014). Urbanization, afforestation, and agricultural activity are the most important anthropogenic forms of LULCC and have important implications for regional climate (Zhang et al., 2013; Chen and Dirmeyer, 2019; Qian et al., 2022). The United Nations Intergovernmental Panel on Climate Change (IPCC) has designated our current understanding of climate forcing due to LULCC as medium to low at the global scale; uncertainties about LULCC forcing at the regional scale can be even greater, especially in developing countries such as China where LULCC in the form of urbanization is unprecedented (Parry et al., 2007; Iacono et al., 2008). Here, we focus on the simulation, qualification and understanding of the effects of LULCC on regional temperature in China over nearly two decades.

In past decades, China has experienced the most rapid expansion of urban areas, accounting for 47.5% of urban area expansion in the world (Sun et al., 2020). Urbanization led to an average temperature increase in China by 1.44 °C during the period of 1961–2013 and contributed to one third of this observed warming among the anthropogenic and natural external forcings (Sun et al., 2016). During urbanization, the urban areas take the place of natural land, can decrease the albedo, increase the surface roughness, may alter the energy partitioning between latent and sensible heat flux (Zhou et al., 2014; Yang et al., 2019; He et al., 2020a). The characteristic of urbanization footprint on climate is the urban heat island effect, the phenomenon of higher temperature in urban areas than rural areas, which has already been identified by both ground measurements and satellite observations (Oke, 1982; Kalnay and Cai, 2003). This effect is interrelated with increasing urban scale, and urban vegetation variations (Zhao et al., 2014; Shen et al., 2021). In addition to urban expansion, urban renewal also occurs in recent years, including the replacement of old houses with high-rise buildings, increasing urban tree cover by the installation of green parks and green roofs (Krayenhoff et al., 2018). Here, vegetation plays an important role in regulating urban temperature shifts. Some studies reported that vegetation degradation with urban expansion in China can exacerbate the urban warming (Peng et al., 2012). However, vegetations increase by urban renewal can reduce urban heat-island effect through shading and evapotranspiration in China (Wang and Shu, 2020; Zhao et al., 2016). Therefore, while both the urban expansion and urban renewal are occurring in Eastern China, the overall impacts of LULCC on regional temperature and the mechanisms underlying them remain elusive.

Attaining an accurate estimate of temperature changes induced by LULCC is a crucial motivation for our study. LULCC-induced temperature changes can be derived with many different approaches. The urban minus rural (UMR) and observation minus reanalysis (OMR) methods are used in surface measurements and satellite observations (Du et al., 2019; Yang et al., 2011). However, these methods have limitations when it comes to the selection of urban pixels and the interpretation of results to separate the albedo effect from the covariation of weather patterns (Chen and Dirmeyer, 2020). In contrast, climate models can adopt different LULCC scenarios to separate their respective temperature responses and have been widely used in previous studies (Liao et al., 2017; Zhao et al., 2019). For example, using landscape data from 1988, 2000, and 2010, Cao et al. (2016) quantified the climate effects of urban expansion in China. Most studies have considered only the effects of urbanization in terms of land type change; changes in vegetation characteristics, which also play an important role in the regional climate, have been largely omitted (Georgescu et al., 2011). The partial consideration of LULCC in above studies leads to an overestimation of temperature increase by accounting only for land type change and not for other land parameters (albedo, green vegetation fraction (GVF), and LAI). In other words, recent realistic variations in land surface may be captured inappropriately in model simulations such as the Weather Research and Forecasting (WRF) model. Therefore, to accurately represent land surface conditions, it is essential to develop the model by incorporating time-varying satellite observations to capture the continuous progression of surface properties associated with LULCC.

In this study, high-resolution and real-time satellite data from 2003 to 2019, including land cover type, albedo, GVF and LAI, are assimilated into WRF to describe the progression of LULCC and to analyze the resulting temperature change. Based on an integrated analysis of regional climate model and satellite observations, this study aims to: (1) develop a WRF model with assimilation of satellite-based land parameters (land cover type, albedo, GVF and LAI) and validation with observation data; (2) quantify the LULCC-induced temperature changes in old urban, new urban and rural areas; and (3) evaluate the biophysical effects of LULCC on surface energy budget. This study focuses on the region of Eastern China (117°E–123°E, 28°N–34°N, Fig. 1) due to the complicated LULCC in this region, including rapid urbanization and agriculture development. We further focus on the summer months because of high urbanization-induced warming effects and active vegetation growth. The paper is organized as follows. The data are described in Section 2. Section 3 is the model development and experiment designs. Section 4 presents the model evaluation, spatiotemporal characteristics of LULCC impact on summer temperature and the analysis of surface energy budget in old urban, new urban and rural areas. The conclusion is presented in Section 5.

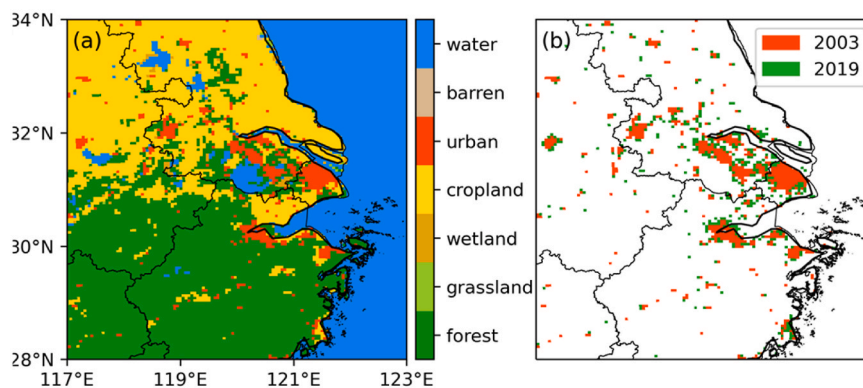


**Fig. 1.** (a) Land cover type over the study domain in 2003. (b) Urban distribution in 2003 (red, old urban areas) and its growth in 2019 (green, new urban areas in 2019).

**Table 1**  
MODIS datasets used in this study.

Parameter	Product	Spatial resolution	Temporal resolution
Land cover type	MCD12Q1	500 m	yearly
Normalized difference vegetation index (NDVI)	MOD13A3	1 km	monthly
Leaf area index (LAI)	MCD15A2H	500 m	8-day
Surface albedo	MCD43A3	500 m	daily
Land surface temperature (LST)	MOD11A1	1 km	daily

## 2. Data

Table 1 lists the MODerate Resolution Imagine Spectroradiometer (MODIS) data products that are integrated with the WRF model, including land cover type, surface albedo, normalized difference vegetation index (NDVI) and LAI. MODIS land surface temperature (LST) data is used for model evaluation, along with surface observations. The time period of this study is 2003–2019 when MODIS/Aqua and MODIS/Terra satellite data are available.

### 2.1. Satellite data assimilated into WRF

MODIS land cover type product (MCD12Q1, Friedl et al., 2002) has a spatial resolution of 500 m (Table 1) and contains 17 land cover types defined by the International Geosphere-Biosphere Program (IGBP) scheme (Table S1). In China, this dataset has a high accuracy of 70% after ignoring the differences of five forest types (Bai et al., 2015). Surface albedo data are from MODIS combined Terra and Aqua bidirectional reflectance distribution function (BRDF) albedo product (MCD43A3). The data include both black-sky albedo ( $\alpha_{BSA}$ , directional-hemispherical reflectance-direct) and white-sky albedo ( $\alpha_{WSA}$ , bihemispherical reflectance-diffuse) in seven spectral bands and three broad bands (visible, 0.3–0.7  $\mu\text{m}$ ; near-infrared, 0.7–5.0  $\mu\text{m}$ ; and shortwave, 0.3–5.0  $\mu\text{m}$ ). It is temporally weighted to the ninth day of every 16 days at 500 m spatial resolution. The uncertainty of MODIS albedo is less than 5% (Cescatti et al., 2012). The blue-sky albedo ( $\alpha_{BLUE}$ , the actual albedo), which is the required input of the WRF model, can be derived from the following equation with an assumed constant white-sky albedo at low solar zenith angles (less than  $70^\circ$ – $75^\circ$ ):

$$\alpha_{BLUE} = \alpha_{BSA}(\theta_{Sun})(1 - S) + \alpha_{WSA}S \quad (1)$$

Here,  $S = 0.2$ , and denotes the diffuse radiation fraction (Ran et al., 2016). Notably, to ensure the accuracy, only the albedo values with quality flag (0–2) are used. The seasonal albedo-averaged maps in the corresponding year are calculated, and then missing values in study area due to cloud contamination or poor-quality data are filled in. The default LAI dataset in WRF model is substituted with MODIS LAI product (MCD15A2H). MODIS LAI is known to have a low uncertainty (0.17) and can better capture the vegetation growth (Ran et al., 2016). GVF is derived from MODIS NDVI product (MOD13A3) in accordance with the algorithm of Purevdorj et al. (1998). Here, NDVI is adopted as an indicator of vegetation variations in this study (Carlson and Ripley, 1997). NDVI (dimensionless) is less than zero for water, and is approximately equal to zero for bare soil, rock and construction area. NDVI is less than 1 for vegetation, and higher NDVI values represent higher vegetation coverage.

### 2.2. Data for validation

Two sets of observational data are used to evaluate the simulation performance. Surface observation site data, derived from the Meteorological Information Comprehensive Analysis and Process System (MICAPS) developed by Chinese National Meteorology Center, has a temporal resolution of 3 h. A map of the 192 surface observation sites over Eastern China is shown in Fig. S1, in which 30 sites are located in

**Table 2**  
WRF configurations in this study.

Physical process	Parameterization scheme
Land surface process	Noah land surface model (Chen and Dudhia, 2001)
Longwave radiation scheme	RRTMG <sup>a</sup> (Iacono et al., 2008)
Shortwave radiation scheme	RRTMG <sup>a</sup>
Planetary boundary layer process	YSU <sup>b</sup> (Hong et al., 2006)
Microphysics scheme	Morrison 2-mom <sup>c</sup> (Morrison et al., 2008)
Cumulus scheme <sup>d</sup>	Grell 3-D (Grell and Dezsó, 2002)

<sup>a</sup> RRTMG, the Rapid Radiative Transfer Model for GCMs.

<sup>b</sup> YSU, the Yonsei University planetary boundary layer scheme.

<sup>c</sup> Morrison 2-mom, Morrison double-moment microphysics scheme.

<sup>d</sup> Only used in the outer domain.

new urban areas in 2019 and the remaining sites are in old urban areas. Additionally, MODIS LST products, MOD11A1 (Terra) Version 6, can provide the spatial pattern of LST for further evaluating the simulation results. LST data are measured at a spatial resolution of 1 km twice a day (~10:30 a.m. and ~10:30 p.m.). Provided by Wan (2014), the LST error is less than 0.5 K. For validation, MODIS LST data are re-gridded into the same spatial resolution as the WRF grids (5 km  $\times$  5 km).

## 3. Method

Model development is conducted to refine various components in WRF to enable MODIS land surface products to be assimilated into WRF every month. Subsequently, the WRF model with the new development, the unified initial conditions from the NASA GEOS global system for WRF land surfaces (hereafter UI-WRF), is configured for two series of numerical experiments to analyze the impact of LULCC on summer temperature in Eastern China. Model simulations are then assessed with surface measurements and satellite observations.

### 3.1. Model development

This study adopts a mesoscale WRF model (Fast et al., 2006; Grell et al., 2005). A Noah land surface model (LSM) scheme is selected for the WRF simulation (Chen and Dudhia, 2001), in which land cover type, GVF, LAI and albedo are key parameters for controlling surface energy partitioning and land-atmosphere interactions. The default land type and GVF in the WRF model are outdated (from the 1990s) (Gutman and Ignatov, 1998; Loveland et al., 2000), while the LAI and albedo values are determined by the prescribed look-up table in the WRF model. They could fail to accurately capture realistic variations of land surface parameters, which result in large errors in model simulations (Li et al., 2014, 2017). In addition, the spatial resolution of these datasets is too coarse (e.g.,  $0.144^\circ \times 0.144^\circ$ ) in the model to describe landscape heterogeneity for high-resolution simulations. Therefore, it is necessary to develop the WRF model by incorporating real-time and high-resolution satellite observations of land parameters (Table 1) and capturing the continuous progression of LULCC. WRF can allow different datasets of land cover type for the LSM, including U.S. Geological Survey (USGS, default), MODIS and the National Land Cover Database (NLCD). Here, 20-class MODIS land type is selected in this study, which contains 17 land cover types defined by IGBP and three classes of tundra (Justice et al., 2002). Several modifications are made in the Noah LSM. First, MODIS land cover type, albedo, GVF, and LAI are resampled and aggregated into monthly mean values, then re-projected and re-gridded into the same resolution as that of the WRF model (25 km, 5 km) and saved at the same data format as that of the geographical data in the model for the areas of interest. The spatial resampling of land cover type is done by nearest-neighbor interpolation, and other parameters are re-sampled with four-pointed bilinear interpolation and grid-cell average interpolation.

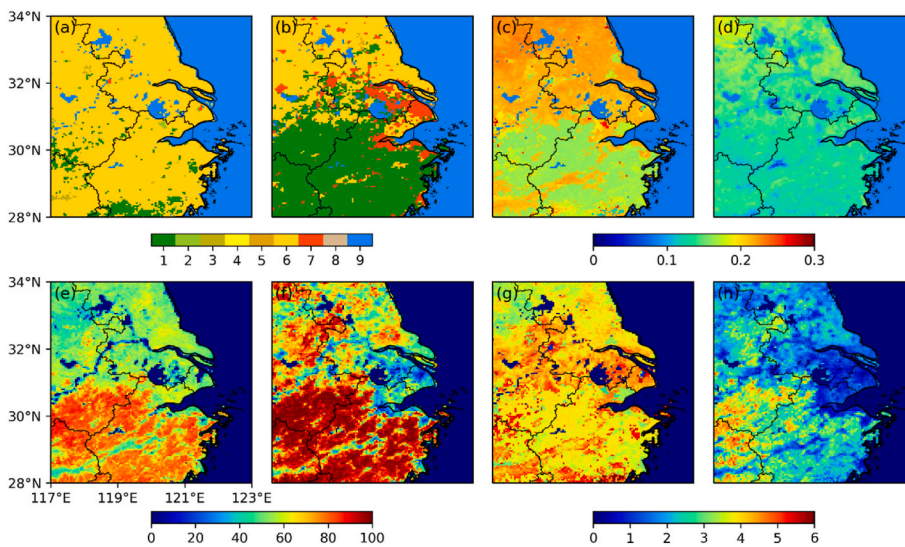


**Fig. 2.** Spatial pattern of (a) USGS land type in 2019-default case and (b) MODIS land type in 2019-modified case. (1–9 corresponding to 9 land type class, 1: forest, 2: shrubland, 3: savanna, 4: grassland, 5: wetland, 6: cropland, 7: urban, 8: barren, 9: water). (c) and (d) show the map of albedo in 2019-default and 2019-modified cases, respectively. Similarly (e) and (f) display the GVF distribution in 2019-default and 2019-modified case, (g) and (h) are LAI in 2019-default and 2019-modified case, respectively. Here, 17 MODIS land cover type were merged into 9 classes to compare with USGS. The forest includes five types of forests: evergreen needleleaf forests, evergreen broadleaf forests, deciduous needleleaf forests, deciduous broadleaf forests and mixed forests. The shrubland includes closed and open shrublands. The savanna includes woody savannas and savannas. The cropland includes cropland/natural vegetation mosaics and croplands.

### 3.2. Model configuration and sensitivity experiments

In this study, model simulations are performed by WRF (version 3.8.1) with modification to enable UI-WRF. Two nested domains over Eastern China are centered around 30.98° N and 120.41° E, with the outer domain at a resolution of 25 km and the inner domain at 5 km (Fig. S1). The model has 47 vertical layers, with 13 levels below 2 km and the lowest level at approximately 130 m. The main physical parameterization schemes are listed in Table 2. It is noted that the cumulus scheme is used only in the outer domain. The 0.625° × 0.5° Modern-Era Retrospective Analysis for Research and Application, Version 2 (MERRA-2) data provide the meteorological initial and boundary condition (Gelaro et al., 2017). The 0.25° × 0.25° Global Land Data Assimilation System (GLDAS) data provide the initial and boundary conditions of soil properties (e.g., soil moisture and temperature) (Rodell et al., 2004).

To examine the influence of LULCC on summer temperature during the period of 2003–2019, UI-WRF experiments are designed for two scenarios as follows: (1) land-constant cases with the same land parameters as 2003 for all years; (2) land-varying cases with monthly land parameters. A detailed description of all simulations performed in this study can be found in Table S2. The simulation captures the spatio-temporal process of urban expansion and vegetation variation in Eastern China for every other year between 2003 and 2019 (2003, 2005, 2007, 2009, 2011, 2013, 2015, 2017, 2019). Here, we focus on the simulation for the month of July to represent mean summertime conditions, as June often is affected by general synoptic conditions with a high cloud cover and frequent rainfall (Zhang et al., 2017). Simulations for the two scenarios are performed using the same physics schemes and meteorology for model boundary conditions, with the only difference being land parameters (land cover type, albedo, GVF, and LAI). The two scenarios use the same 17-category soil texture map from the 5 min United Nations/Food and Agriculture Organization database (Chen and Dudgeon, 2001), assuming that the soil type has little change associated with the urban expansion. The remaining secondary surface parameters (e.g., roughness length) are assigned by tabulated values according to land type, GVF and soil index in WRF model. Simulations are conducted from June 28 to July 31 in the corresponding year, and only data in July are adopted for the following analyses. The effect of LULCC on temperature is quantified as the difference in temperature between the land-varying and land-constant cases for each year relative to 2003. In this way, the geospatial evolution of LULCC effects on temperature since 2003 can be analyzed for each year. The model output data is archived for every hour.

To assess the performance of the UI-WRF modified model, an additional sensitivity test, 2019-default, is conducted, along with the 2019-modified case (one of the land-varying cases performed for July 2019). For the 2019-default case, the land parameters are set as the WRF Noah default values. The comparisons of two land parameters are shown in Fig. 2. Then the simulated temperature of 2019-default and 2019-modified are both compared with surface observations and MODIS LST to evaluate the model performance.

### 3.3. The definition of old urban, new urban and rural areas

To explore the disparity of temperature, the urban areas are further divided into old urban areas and new urban areas. Based on MODIS land cover type data, urban areas that existed in the initial year of 2003 (Fig. 1b, red) are regarded as old urban areas, while the newly urbanized grid cells after 2003 are new urban areas (Fig. 1b, green). New urban areas vary in time and Fig. S2 portrays the spatial pattern of new urban areas with urban expansion for every other year from 2005 to 2019. The remaining non-urban grid cells (excluding water grid cells) are referred as rural areas. Rural areas include cropland and forest areas. Further, rural areas in the range of 5–20 km (equivalent to 1–4 grid cells at the spatial resolution of 5 km in the model) away from new urban grid cell are defined as suburbs (Fig. S3). All of these areas are derived from land-varying cases and identified by model grids with the spatial resolution of 5 km, in which new urban, suburb and rural areas change over time, but old urban areas remain unchanged. As shown in Fig. 1, urban area proportion increased from 4.02% in 2003 to 6.60% in 2019 with the growth rate of 64.31%. Eastern China's urbanization is accompanied by a decrease in cropland and forest cover, which accounting for 39% and 27.3% of our study domain area in 2003, respectively. Among the approximately 10<sup>5</sup> km<sup>2</sup> of natural land converted to urban areas, 52.6% is forest and 45.4% is cropland (Fig. S4). Croplands (forests) and urban areas have clearly different land parameters, with urban areas having lower albedo and NDVI values than the rural areas. The difference in land parameters can further influence the temperature changes and regional energy surface budget.

Growth rate (GR) is used to quantify the magnitude of urban expansion (at the expanses of total rural areas) from 2003 to 2019.

$$GR = \frac{A_{2019} - A_{2003}}{A_{2003}} \quad (2)$$

$A_{2003}$  and  $A_{2019}$  denote the area of urban areas in 2003 and 2019, respectively.

**Table 3**

Performance statistics for WRF-simulated 2 m temperature ( $T_2$ ) in 2019-default and 2019-modified cases, including mean bias (MB), mean error (ME) and Root-Mean-Square-Error (RMSE).

Index <sup>a</sup>	2019-default (all domain)	2019-modified (all domain)	2019-default (new urban areas)	2019-modified (new urban areas)
MB <sup>b</sup>	-0.80	0.23	-0.89	0.20
ME <sup>c</sup>	1.81	1.58	1.90	1.43
RMSE <sup>d</sup>	2.21	1.85	2.28	1.75

<sup>a</sup> In the equations, *sim* and *obs* represent the simulated and observed temperature, and *N* is the number of data pairs at all the observation sites.

$$^b MB = \frac{1}{N} \sum_{i=1}^N (sim_i - obs_i).$$

$$^c ME = \frac{1}{N} \sum_{i=1}^N |sim_i - obs_i|.$$

$$^d RMSE = \sqrt{\frac{1}{N} \sum_{i=1}^N (sim_i - obs_i)^2}.$$

### 3.4. Surface energy budget

The changes in surface land temperature (TSK) and air temperature due to LULCC are closely related with the individual terms of the surface energy balance.

$$R_n = LE + H + G = SW_{net} + LW_{net} \tag{3}$$

$$SW_{net} = SW_{down} - SW_{up} = (1 - \alpha)SW_{down} \tag{4}$$

$$LW_{net} = LW_{down} - LW_{up} = LW_{down} - \epsilon\sigma TSK^4 \tag{5}$$

Where  $R_n$  is the net radiation,  $H$  is the sensible heat flux,  $LE$  is the latent heat flux,  $G$  is the ground heat flux.  $SW_{net}$  and  $LW_{net}$  are net shortwave and longwave radiation, respectively.  $SW_{down}$  ( $SW_{up}$ ) denotes the downward (upward) shortwave radiation. Similarly,  $LW_{down}$  ( $LW_{up}$ ) is the downward (upward) longwave radiation.  $A$  is the surface albedo,  $\epsilon$  is emissivity,  $\sigma$  is the Stephan-Boltzmann constant ( $5.67 \times 10^{-8} \text{ W m}^{-2} \text{ K}^{-4}$ ),  $TSK$  is land surface temperature in the Eq. (5).

The impacts of LULCC on temperature and surface energy budget are

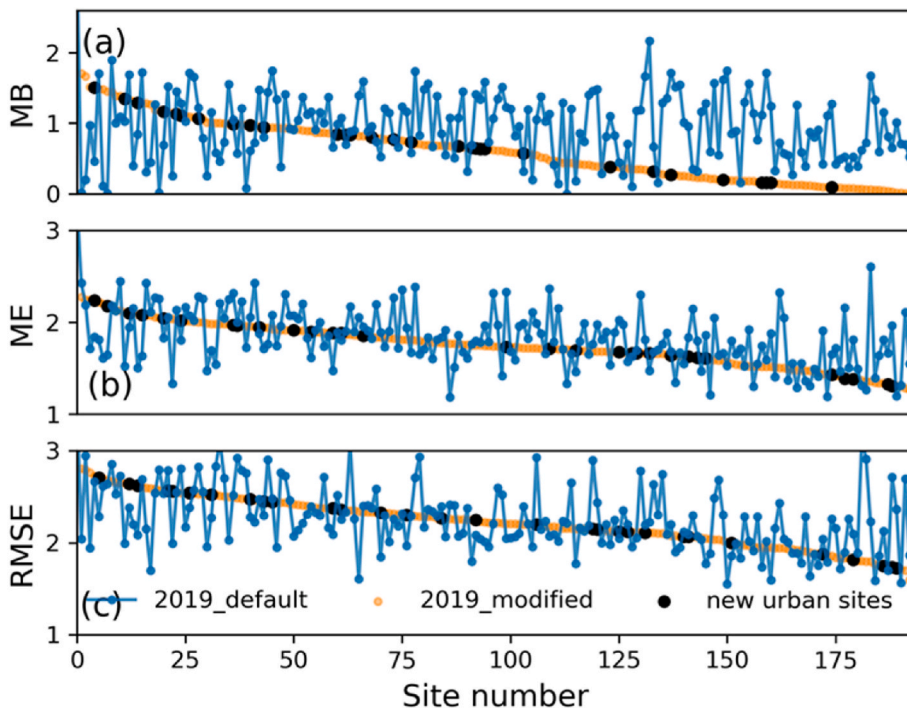


**Fig. 3.** (a) MB (Mean Bias), (b) ME (Mean Error) and (c) RMSE (Root-Mean-Square-Error) in simulated temperatures for 2019-default (blue line) and 2019-modified (orange line) cases at 192 surface stations. MB is shown as absolute value for comparison here. The x-axis is the station number sorted by the quantity shown in each panel for 2019-modified case. The orange/black dots below (above) blue dots indicate an improvement (degradation) in 2019-modified compared to 2019-default case. Black dots denote new urban sites.

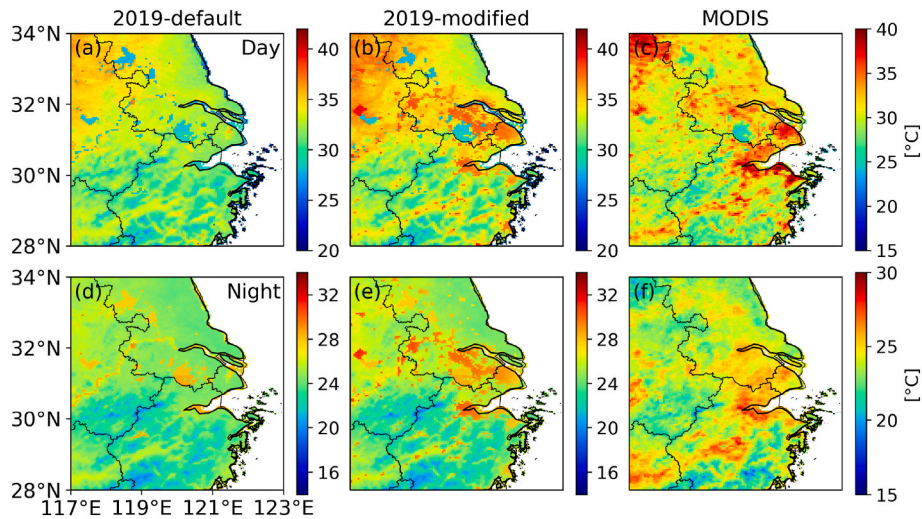
calculated as the difference of the variables (temperature, albedo, heat flux, etc.) simulated by two experiments (land-varying-- land-constant cases). These differences are examined by two-tailed Student's tests, and  $p < 0.05$  indicates the difference is statistically significant.

## 4. Results

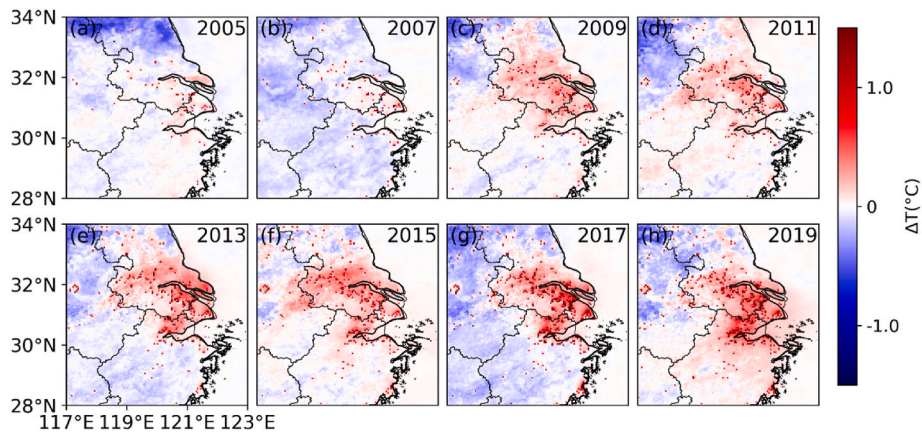
### 4.1. Model evaluation

Fig. 2 shows the comparison of land parameters (land cover type, albedo, GVF, and LAI) in 2019-default and 2019-modified cases. Two land type maps (Fig. 2a and b) from 2019-default and 2019-modified case reveal that Eastern China experienced dramatic urbanization during the past 20 years, and large growth of forests in the South with the removal of cropland. As shown in Fig. 2c and d, MODIS albedo in 2019-modified can portray that urban and forests have slightly lower albedo than northern cropland, while tabulated albedo in 2019-default (without using MODIS-based data) is not representative. MODIS GVF (Fig. 2e and f) and LAI (Fig. 2g and h) in 2019-modified can reproduce high values over the southern forests, and lower values over northern croplands and urban areas compared with 2019-default. These land parameters in 2019-modified can provide more reliable land characteristics than 2019-default, which favors a better simulation of temperature. Then surface observations and MODIS LST are both used to evaluate the simulated temperature and model performance of 2019-default and 2019-modified.

Model performance is evaluated through comparison with surface and satellite-based measurements of temperature. Table 3 lists the comparison statistics between surface observations and the 2019-default (as well as 2019-modified) cases. In monthly averages, 2019-modified performs better than 2019-default in all sites (192 sites), especially in new urban sites (30 sites) with the absolute value of mean bias (MB) reduced from  $-0.89$  to  $0.20$  °C, Mean Error (ME) from  $1.90$  to  $1.43$  °C, and Root-Mean-Square-Error (RMSE) from  $2.28$  to  $1.75$  °C. Fig. 3 further displays the comparisons of ME, MB and RMSE at each observation station for the 2019-default (blue line) and 2019-modified (orange) cases. Black dots denote new urban sites in 2019-modified. For comparison, the x-axis is the observation site number sorted by the quantity



**Fig. 4.** The comparisons among simulated surface temperature (TSK) in (a) 2019-default, (b) 2019-modified and (c) MODIS Land Surface Temperature (LST) during the daytime of Terra satellite overpass time (unit: °C). (d–f) are similar with (a–c) but for the nighttime. Note, (c) and (f) are satellite data for clear-sky only, while model data (a,b,d,e) are for all-skies.



**Fig. 5.** Spatial pattern of LULCC-induced the monthly mean air temperature difference ( $\Delta T_2$ , land-varying case – land-constant case, unit: °C) for (a) 2005, (b) 2007, (c) 2009, (d) 2011, (e) 2013, (f) 2015, (g) 2017 and (h) 2019, respectively.

shown in each panel for the 2019-modified case. Orange/black dots below blue dots indicate that the bias of simulated temperature in 2019-modified is lower than that of 2019-default; this represents an improvement in 2019-modified. MB, ME, and RMSE are improved in ~72%, ~65%, and ~58% of all observation sites over the study domain, respectively. For new urban sites (black dots), MB, ME, and RMSE are improved in ~87%, ~83%, and ~73%, respectively.

To further evaluate the model simulation, the monthly averages of simulated surface temperature (TSK) are compared with MODIS LST observations. Compared to 2019-default (Fig. 4a and d), 2019-modified (Fig. 4b and e) can reproduce the hot spots of temperature in urban areas (e.g., Shanghai, Nanjing, Hangzhou), and is in better agreement with MODIS (Fig. 4c and f) during the daytime and nighttime overpass of the

satellite. The pattern correlation coefficient (PCC) between 2019-modified and MODIS is 0.68 during daytime and 0.63 during nighttime, which is higher than the counterparts (0.52 both in daytime and nighttime) for 2019-default. Overall, UI-WRF model substantially reduces the bias of simulated temperature after the inclusion of satellite-based land parameters. The more accurate simulations can ultimately improve the assessment of LULCC impact on temperature in the next step.

#### 4.2. LULCC impact on temperature and vegetation variations

Fig. 5 and Fig. S5 portray the spatial pattern of LULCC-induced mean 2-m temperature ( $\Delta T_2$ ) and land surface temperature ( $\Delta TSK$ ) differences

**Table 4**

Averages of variable differences calculated in old urban, new urban and rural areas (identified by model land type in 2019) between 2019 and 2003, including albedo ( $\Delta albedo$ , land-varying case–land-constant case), NDVI ( $\Delta NDVI$ ), land surface temperature ( $\Delta TSK$ , °C), air temperature ( $\Delta T_2$ , °C), net radiation ( $\Delta R_n$ , W/m<sup>2</sup>), latent heat flux ( $\Delta LE$ , W/m<sup>2</sup>), sensible heat flux ( $\Delta H$ , W/m<sup>2</sup>) and ground heat flux ( $\Delta G$ , W/m<sup>2</sup>).

	$\Delta albedo$	$\Delta NDVI$	$\Delta TSK$	$\Delta T_2$	$\Delta R_n$	$\Delta LE$	$\Delta H$	$\Delta G$
old urban areas	−0.0008	0.0233	0.13	0.10	−1.09	0.29	−1.20	−0.18
new urban areas	−0.0023	−0.0499	3.40	1.69	−47.36	−99.33	66.18	−14.21
rural areas	0.0013	0.0381	−0.03	−0.02	0.41	0.85	−0.55	0.11

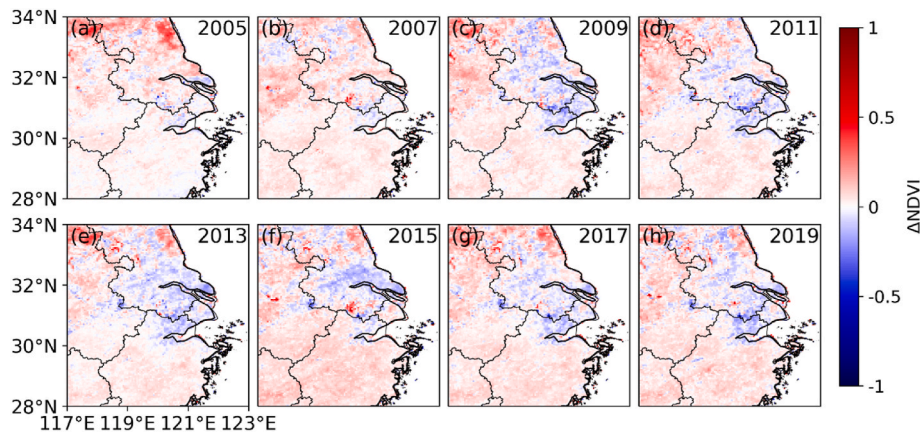


Fig. 6. Similar with Fig. 5, but for  $\Delta NDVI$ .

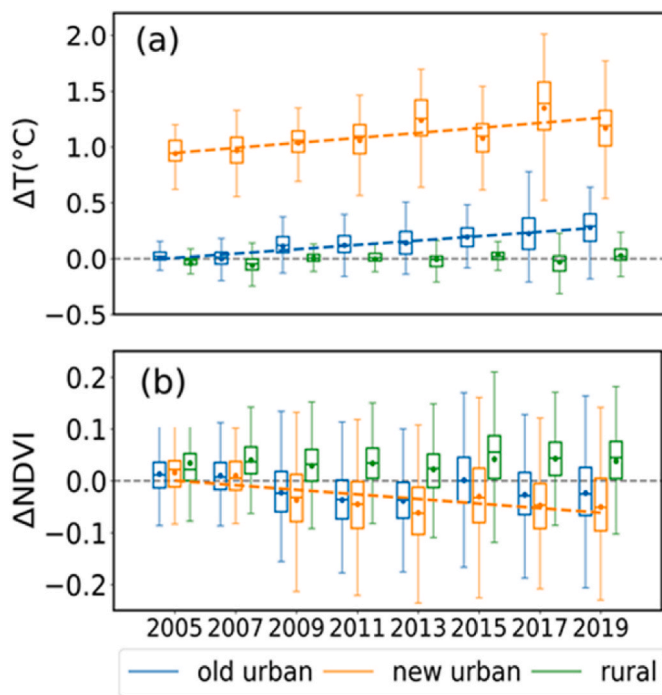


Fig. 7. (a) The boxplots of temperature difference ( $\Delta T_2$ , land-varying case – land-constant case, unit:  $^{\circ}\text{C}$ ) in old urban (blue), new urban (orange) and the rural areas (green) from 2005 to 2019, respectively. (b) is for the NDVI difference ( $\Delta NDVI$ ). The dashed lines represent the temporal trend is significant ( $p < 0.01$ ).

during the period of 2005 and 2019, which show the urban warming and rural cooling effect. The magnitude of  $\Delta T_{SK}$  is obviously greater than  $\Delta T_2$ , even exceeding  $2^{\circ}\text{C}$  in dramatic urbanization areas. The areas of urban warming expand as urban size increases and grows as part of various urban clusters. According to Fig. S2 and Fig. 5, new urban areas experience a greater temperature increase ( $>1^{\circ}\text{C}$ ) compared to old urban areas. It is calculated that old urban areas experience a  $0.13^{\circ}\text{C}$  ( $0.10^{\circ}\text{C}$ ) increase in  $T_{SK}$  ( $T_2$ ), while new urban areas experience a  $3.40^{\circ}\text{C}$  ( $1.69^{\circ}\text{C}$ ) increase in 2019 compared with 2003 (Table 4). Moreover, new urban areas also have a more significant increasing trend of  $\Delta T_2$  with a mean value of  $0.04^{\circ}\text{C}$  every two years, compared with old urban areas ( $0.02^{\circ}\text{C}$ , Fig. 7a). Nevertheless, old urban areas are still warmer than new urban areas (Fig. 8a). With the temperature in new urban areas grows faster, a significant decreasing trend is found in the difference of temperature between the old and new urban areas

(Fig. 8b). In rural areas, LULCC produces a noticeable cooling effect, with  $T_{SK}$  ( $T_2$ ) decreasing by  $0.03^{\circ}\text{C}$  ( $0.02^{\circ}\text{C}$ ). Specifically, LULCC reduces  $T_{SK}$  ( $T_2$ ) by  $0.06^{\circ}\text{C}$  ( $0.01^{\circ}\text{C}$ ) in cropland, which is significantly greater than  $-0.02^{\circ}\text{C}$  ( $0^{\circ}\text{C}$ ) of  $T_{SK}$  ( $T_2$ ) in forest areas. The temperature in rural areas appears to have no linear temporal trend and fluctuates around zero (Fig. 7a), implying that rural cooling effect is not enhanced with time.

Vegetation variations due to LULCC also occur in Eastern China. Urban areas become less green while rural areas become greener as indicated by NDVI, particularly in northern croplands in recent years (Fig. 6). Table 4 shows that NDVI decreases in new urban areas ( $-0.05$ ) because new urban areas are developed with the loss of natural land during urban expansion. The significant decreasing trend of  $\Delta NDVI$  in new urban areas with the trend of  $-0.009$  every two years (Fig. 7b), indicates that new urban areas become less green during past years. In old urban areas, satellite evidences show an increase in NDVI (Table 4) in 2019 compared with 2003. These can be attributed to the urban renewal over Eastern China in recent years. According to Wang and Shu (2020), the replacement of the old shorter buildings with high-rise buildings can significantly change the albedo in old urban areas, and more scattered greenspaces can increase the NDVI in old urban areas of Shanghai based on high-resolution satellite data. Our results show that  $\Delta NDVI$  fluctuates with no decreasing linear trend in old urban areas, thanks in part to the vegetation restoration during urban renewal in recent years (Fig. 8c). Overall, the disparity of NDVI between old and new urban areas is also significantly decreased, just like the temperature, even though new urban areas are still greener than old urban areas (Fig. 8). In rural areas, NDVI overall increases by  $0.04$ , with the increase more in croplands ( $0.05$ ) than in forests ( $0.02$ ). NDVI variations in rural areas can be influenced by local climate and agricultural practices, such as the irrigation, wheat harvest and straw burning (Aegerter et al., 2017; Guo et al., 2016; Wang et al., 2017). As illustrated in Figs. 5–7, the spatio-temporal changes of NDVI have a negative phase with temperature, that is, the area of vegetation loss resonates the area of urban warming, while increased vegetation in rural areas can enhance the cooling effect by increasing evapotranspiration. They all indicate that vegetations play an important role in regulating urban temperature shifts.

In addition to urban areas, the urbanization can also have an additional warming effect on suburbs. To capture this change,  $\Delta T_2$  and  $\Delta NDVI$  are calculated for suburb grid cells, with the ranges of 5–10 km (1–2 model grid cells), 10–15 km (2–3 grid cells) and 15–20 km (3–4 grid cells) away from each new urban grid cell (Fig. 9). The warming of suburbs occurred beginning in 2009 due to urban expansion, with no warming influence from 2005 to 2007 ( $\Delta T_2 < 0$ , Fig. 9a). Similar to temperature increases, urbanization also reduces the greenness beginning in 2009 ( $\Delta NDVI < 0$ , Fig. 9b). Furthermore, suburb warming is reduced (Fig. 9), as one moves away from new urban areas and more

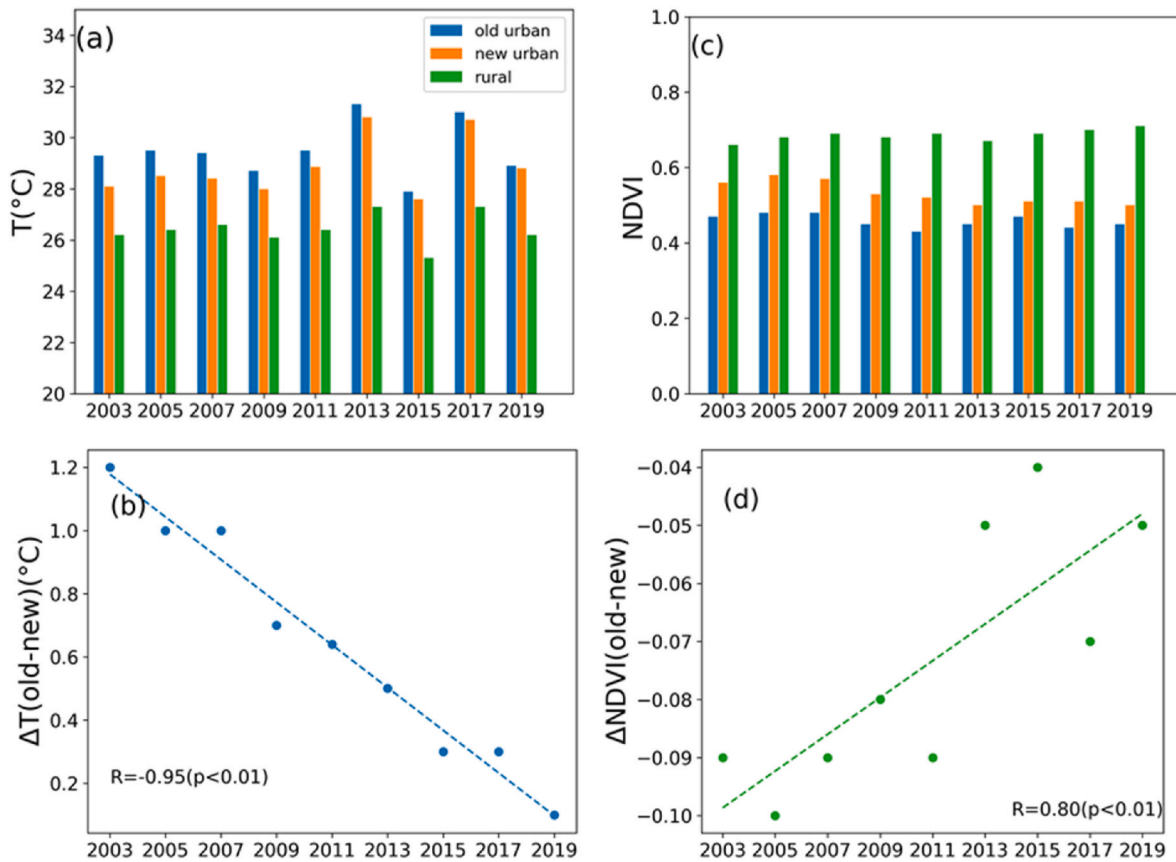


**Fig. 8.** (a) The monthly mean temperature in old urban, new urban and rural areas (unit: °C), (b) is the difference of temperature between old and new urban areas as a function of time, (c) and (d) are similar with (a) and (b) respectively, but for NDVI. Note that the blue line in (b) denotes the significant decreasing trend in the difference of temperature between old and new urban areas, the green line in (d) is also the significant decreasing trend in the difference of NDVI.

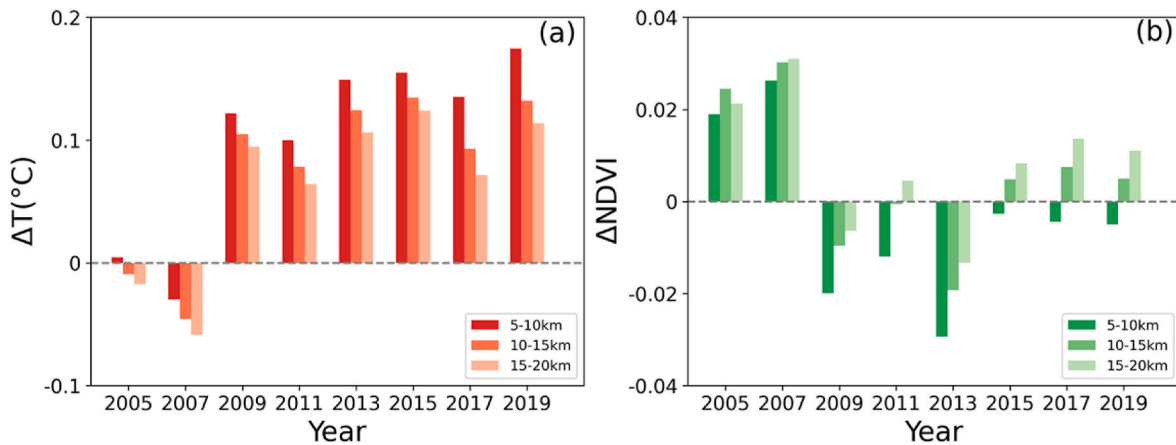


**Fig. 9.** (a) Mean temperature difference ( $\Delta T_2$ , unit: °C) for suburbs which are in the range of 5–10 km (equivalent to 1–2 model grid cells at the spatial resolution of 5 km in WRF model, dark red), 10–15 km (2–3 grid cells, red) and 15–20 km (3–4 grid cells, light red) away from new urban areas from 2005 to 2019. (b) is mean NDVI difference ( $\Delta NDVI$ ), dark green represents the suburbs which are in the range of 5–10 km (1–2 model grid cells), green is 10–15 km (2–3 grid cells) and light green is 15–20 km (3–4 grid cells).

vegetation is restored. In recent years, vegetation has increased within 10–20 km (2–4 grid cells) of new urban areas (e.g.,  $\Delta NDVI > 0$  in green, light green bars during 2015, 2017, 2019), and may attenuate the urban warming effect to some extent. In general, from 2003 to 2019, temperature ( $T_2$ ) rises by 0.17 °C (5–10 km), 0.13 °C (10–15 km) and 0.11 °C (15–20 km). Meanwhile, NDVI decreases accordingly with away from new urbans. As a result, urban sprawl can warm areas in close proximity to new urban areas, with decreasing greenspace. In all three

ranges away from new urban areas, there is a significant increasing trend of mean temperature difference of 0.026 °C, 0.022 °C, and 0.020 °C every two years, respectively. It indicates that as the size of cities grows, so does the warming effect (including its spatial coverage).

#### 4.3. LULCC impact on surface energy budget

To explore the correspondence between temperature and surface

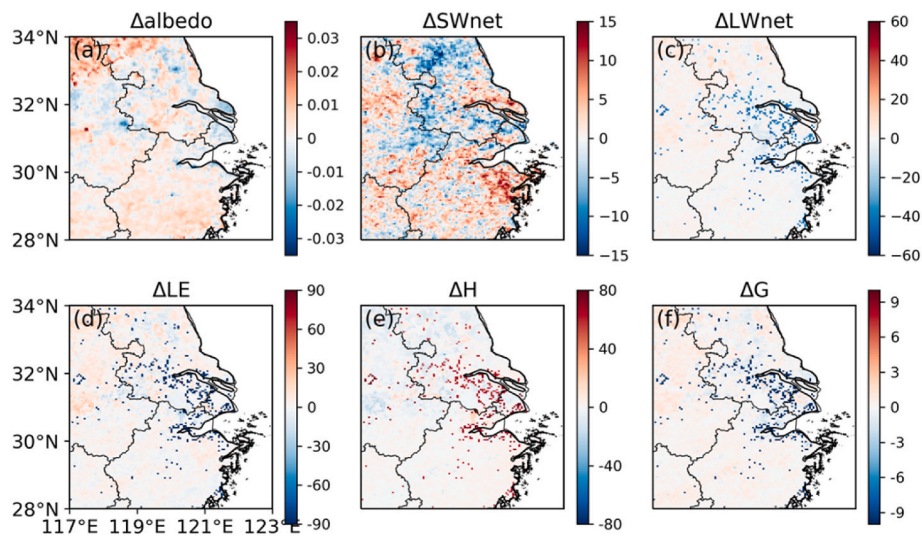


**Fig. 10.** Spatial pattern of LULCC-induced the monthly mean albedo and heat flux ( $\Delta Heat\ flux$ , land-varying case–land-constant case, unit:  $W\ m^{-2}$ ) difference during 2019 for (a)  $\Delta albedo$ , (b)  $\Delta SW_{net}$  (net shortwave radiation), (c)  $\Delta LW_{net}$  (net shortwave and longwave radiation), (d)  $\Delta LE$  (latent heat flux), (e)  $\Delta H$  (sensible heat flux), (f)  $\Delta G$  (ground heat flux).

energy budget, their respective changes (in form of  $\Delta Heat\ flux$ ) due to LULCC are shown in Fig. 10. The conversion of natural land to impervious surface in new urban areas can cause notable perturbations to the surface energy balance, the magnitude of  $\Delta Heat\ flux$  in new urban areas is obviously much greater than that in old urban and rural areas, where the land type remains unchanged. In new urban areas, owing to reduced albedo (Table 4 and Fig. 10a) in new urban areas,  $SW_{up}$  decreases and  $SW_{net}$  can increase (Eq. (4)). An increase in  $TSK$  causes an increase in  $LW_{up}$  (Eq. (5)), moreover,  $LW_{down}$  also increases due to higher  $T_2$  induced by urbanization. Taking shortwave (Fig. 10b) and longwave radiations (Fig. 10c) together,  $R_n$  decreases accordingly with the value of  $-47.36\ W\ m^{-2}$  (Table 4). New urban areas have higher fractions of impervious surface with less vegetation cover compared with before, and it cause a much decrease in  $LE$  ( $-99.23\ W\ m^{-2}$ , Table 4 and Fig. 10d) and the increase in  $H$  ( $66.18\ W\ m^{-2}$ ), along with the decrease in  $G$  ( $-14.21\ W\ m^{-2}$ ). In this process,  $\Delta LE$  is much higher than other terms, which implies that the decreased latent heat dominates the biophysical warming effect in new urban areas.

As illustrated in Table 4 and Fig. 10, in old urban areas,  $R_n$  decreased ( $-1.09\ W\ m^{-2}$ ) due to a decline in albedo. Increased  $LE$  ( $0.29\ W\ m^{-2}$ ) may result from an increase in NDVI in recent years due to urban renewal and a decrease in  $H$  ( $-1.20\ W\ m^{-2}$ ) is probably attributed to the decline in surface wind speed during the past decades as a result of urbanization (Zhang and Wang, 2021). In rural areas, increased NDVI ( $0.04$ , Table 4) can promote the transpiration rate, leading to higher  $LE$  ( $0.85\ W\ m^{-2}$ ) and lower  $H$  ( $-0.55\ W\ m^{-2}$ ); hence, LULCC has cooling and wetting effects in rural areas, and the increase in  $LE$  due to rural greenness dominates the rural cooling.

In addition, the warming in old urban areas and suburbs may be mainly associated with the heat convections from new urban areas, which is quantified by aerodynamic resistance (Zhao et al., 2014). The convection efficiency between urban and rural areas is suggested to dominate the temperature difference between urban and the surrounding rural areas especially in humid areas. More observation data and modeling are needed to explore the possible mechanism in old urban areas, which is worthy of more attention in our future study. Aside from the factors mentioned above, anthropogenic heat release, which is not considered in our study, is also a contributor to urban warming. According to the model simulation conducted by Liao et al. (2017), anthropogenic heat can cause a  $0.6\ ^\circ C$  warming in Eastern China. Taking this into account, the temperature rise over old urban areas is still less than that over new urban areas.

## 5. Conclusions and discussion

In this study, satellite observations are integrated into the WRF model to investigate the progression of LULCC-induced urban warming and rural cooling during the past two decades. To accurately capture the continuous progression of LULCC, MODIS land surface products (land cover type, albedo, GVF, and LAI) are assimilated into UI-WRF. This assimilation leads to the improvement in 2-m temperature, the corresponding ME, MB, and RMSE in  $\sim 72\%$ ,  $\sim 65\%$  and  $\sim 58\%$  of observation sites during July 2019. Compared with satellite data, 2019-modified case with data assimilation can better capture the urban heat island during daytime and nighttime than 2019-default case without data assimilation. These evaluation results provide the fidelity needed to use UI-WRF as a tool to study the impact of LULCC on surface temperature in 2003–2019, both spatially and temporally.

Subsequently, two sets of WRF simulations are performed for land-constant and land-varying cases every two years between 2003 and 2019. The model results show that LULCC causes urban areas to become warmer, with the effect being more pronounced in new urban areas than in old urban areas. New urban areas have an increase of  $1.69\ ^\circ C$  ( $3.40\ ^\circ C$ ) in  $T_2$  ( $TSK$ ), old urban areas have a slight increase of  $0.10\ ^\circ C$  ( $0.13\ ^\circ C$ ) in  $T_2$  ( $TSK$ ). Significant vegetation degradation is found during new urban development, with a significant decreasing trend in NDVI. However, vegetation restoration is also found in old urban areas in recent years due to urban renewal. Furthermore, the difference of new urban and old urban temperature is becoming smaller with time during 2003–2019. On the other hand, LULCC cools and greens rural areas, rendering a  $0.03\ ^\circ C$  ( $0.02\ ^\circ C$ ) decrease in  $TSK$  ( $T_2$ ) and an increase in NDVI ( $0.04$ ). In addition, urbanization warming doesn't stay in urban areas, and can be extended to the suburbs. The urban warming along with vegetation degradation can reach to the suburbs within 20 km from the outskirts of urban areas. The analysis of surface energy budget further reveals that the reduction in latent heat is the dominant factor contributing to the warming over new urban areas and cooling in rural areas.

Our satellite-based analysis and regional modeling reveal the internal dynamics of temperature in urban areas due to urban expansion and urban renewal. These findings show that the brand new urban areas are hotspots for urban management, and more greenspace and albedo management are suggested in future landscape plans. Effective measures for urban restoration are suggested, such as increasing tree cover, expanding urban park space (especially for medium-density urban

areas), and adopting green or cool roofs (especially for high-density and commercial areas, as stated by Krayenhoff et al. (2018) and He et al. (2020b)). In Shanghai, approximately 20 million m<sup>2</sup> of roof space is available and suitable for roof greening, which would help to ameliorate future warming temperatures (Shanghai Bureau of Statistics, 2017). Therefore, future LULCC policy should include efforts to increase more vegetation and albedo management in both old and new urban areas across Eastern China to alleviate urban warming.

### CRedit authorship contribution statement

**Yanyu Wang:** Conceptualization, Methodology, Formal analysis, Writing – original draft, Funding acquisition. **Jun Wang:** Conceptualization, Writing – review & editing. **Huanxin Zhang:** Formal analysis, Writing – review & editing. **Nathan Janecek:** Formal analysis, Writing – review & editing. **Yi Wang:** Formal analysis. **Meng Zhou:** Formal analysis. **Pengke Shen:** Methodology, Formal analysis. **Jianguo Tan:** Writing – review & editing. **Qianshan He:** Data curation, Writing – review & editing, Funding acquisition. **Tiantao Cheng:** Writing – review & editing, Funding acquisition. **Cheng Huang:** Writing – review & editing.

### Declaration of competing interest

The authors declare that they have no known competing financial interests or personal relationships that could have appeared to influence the work reported in this paper.

### Data availability

MODIS satellite data used in this study are available at Earthdata (<https://earthdata.nasa.gov/>). Temperature observation data from MICAPS is provided by Chinese National Meteorology Center (<http://www.micaps.cn/>).

### Acknowledgments

This research is supported by the Science and Technology Commission of Shanghai Municipality (22YF1438200), the China Postdoctoral Science Foundation (2022M712145), the National Natural Science Foundation of China (42175179, 41775019 and 41801367). Yanyu Wang gratefully acknowledges the support from the China Scholarship Council (201906100125). Jun Wang acknowledges in-kind support from the University of Iowa.

### Appendix A. Supplementary data

Supplementary data to this article can be found online at <https://doi.org/10.1016/j.atmosenv.2023.119850>.

### References

Aegerter, C., Wang, J., Ge, C., Irmak, S., Oglesby, R., Wardlow, B., Yang, H., You, J., Shulski, M., 2017. Mesoscale modeling of the meteorological impacts of irrigation during the 2012 central plains drought. *J. Appl. Meteorol. Climatol.* 56, 1259–1283.

Bai, Y., Feng, M., Jiang, H., Wang, J.L., Liu, Y.Z., 2015. Validation of land cover maps in China using a sampling-based labeling approach. *Rem. Sens.* 7, 10589–10606.

Cao, Q., Yu, D., Georgescu, M., Wu, J., 2016. Impacts of urbanization on summer climate in China: an assessment with coupled land-atmospheric modeling. *J. Geophys. Res. Atmos.* 121 (10), 505–510, 521.

Carlson, T.N., Ripley, D.A., 1997. On the relation between NDVI, fractional vegetation cover, and leaf area index. *Remote Sens. Environ.* 62, 241–252.

Cescatti, A., Marcolla, B., Vannan, S.K.S., Pan, J.Y., Roman, M.O., Yang, X.Y., Ciaia, P., Cook, R.B., Law, B.E., Matteucci, G., Migliavacca, M., Moors, E., Richardson, A.D., Seufert, G., Schaaf, C.B., 2012. Intercomparison of MODIS albedo retrievals and in situ measurements across the global FLUXNET network. *Remote Sens. Environ.* 121, 323–334.

Chen, F., Dudhia, J., 2001. Coupling an advanced land surface-hydrology model with the Penn State-NCAR MM5 modeling system. Part I: model implementation and sensitivity. *Mon. Weather Rev.* 129, 569–585.

Chen, L., Dirmeyer, P.A., 2019. The relative importance among anthropogenic forcings of land use/land cover change in affecting temperature extremes. *Clim. Dynam.* 52, 2269–2285.

Chen, L., Dirmeyer, P.A., 2020. Reconciling the disagreement between observed and simulated temperature responses to deforestation. *Nat. Commun.* 11, 1–10.

Du, J., Wang, K., Jiang, S., Cui, B., Wang, J., Zhao, C., Li, J., 2019. Urban dry island effect mitigated urbanization effect on observed warming in China. *J. Clim.* 32, 5705–5723.

Fast, J.D., Gustafson, W.I., Easter, R.C., Zaveri, R.A., Barnard, J.C., Chapman, E.G., Grell, G.A., Peckham, S.E., 2006. Evolution of ozone, particulates, and aerosol direct radiative forcing in the vicinity of Houston using a fully coupled meteorology-chemistry-aerosol model. *J. Geophys. Res. Atmos.* 111.

Friedl, M.A., McIver, D.K., Hodges, J.C.F., Zhang, X.Y., Muchoney, D., Strahler, A.H., Woodcock, C.E., Gopal, S., Schneider, A., Cooper, A., Baccini, A., Gao, F., Schaaf, C., 2002. Global land cover mapping from MODIS: algorithms and early results. *Remote Sens. Environ.* 83, 287–302.

Gelaro, R., McCarty, W., Suarez, M.J., Todling, R., Molod, A., Takacs, L., Randles, C.A., Darmenov, A., Bosilovich, M.G., Reichle, R., Wargan, K., Coy, L., Cullather, R., Draper, C., Akella, S., Buchard, V., Conaty, A., da Silva, A.M., Gu, W., Kim, G.K., Koster, R., Lucchesi, R., Merkova, D., Nielsen, J.E., Partyka, G., Pawson, S., Putman, W., Rienecker, M., Schubert, S.D., Sienkiewicz, M., Zhao, B., 2017. The Modern-Era Retrospective analysis for research and applications, version 2 (MERRA-2). *J. Clim.* 30, 5419–5454.

Georgescu, M., Lobell, D.B., Field, C.B., 2011. Direct climate effects of perennial bioenergy crops in the United States. *Proc. Natl. Acad. Sci. U. S. A.* 108, 4307–4312.

Grell, G.A., Dezsó, D., 2002. A generalized approach to parameterizing convection combining ensemble and data assimilation techniques. *Geophys. Res. Lett.* 29, 1693.

Grell, G.A., Peckham, S.E., Schmitz, R., McKeen, S.A., Frost, G., Skamarock, W.C., Eder, B., 2005. Fully coupled "online" chemistry within the WRF model. *Atmos. Environ.* 39, 6957–6975.

Guo, W., Wang, X., Sun, J., Ding, A., Zou, J., 2016. Comparison of land-atmosphere interaction at different surface types in the mid- to lower reaches of the Yangtze River valley. *Atmos. Chem. Phys.* 16, 9875–9890.

Gutman, G., Ignatov, A., 1998. The derivation of the green vegetation fraction from NOAA/AVHRR data for use in numerical weather prediction models. *Int. J. Rem. Sens.* 19, 1533–1543.

He, C., Zhou, L.G., Yao, Y.R., Ma, W.C., Kinney, P.L., 2020a. Estimating spatial effects of anthropogenic heat emissions upon the urban thermal environment in an urban agglomeration area in East China. *Sustain. Cities Soc.* 57.

He, C., Zhao, J.R., Zhang, Y., He, L., Yao, Y.R., Ma, W.C., Kinney, P.L., 2020b. Cool roof and green roof adoption in a metropolitan area: climate impacts during summer and winter. *Environ. Sci. Technol.* 54, 10831–10839.

Hong, S.Y., Noh, Y., Dudhia, J., 2006. A new vertical diffusion package with an explicit treatment of entrainment processes. *Mon. Weather Rev.* 134 (9), 2318.

Iacono, M.J., Delamere, J.S., Mlawer, E.J., Shephard, M.W., Clough, S.A., Collins, W.D., 2008. Radiative forcing by long-lived greenhouse gases: calculations with the AER radiative transfer models. *J. Geophys. Res. Atmos.* 113 (D13).

Justice, C.O., Townshend, J.R.G., Vermote, E.F., Masuoka, E., Wolfe, R.E., Saleous, N., Roy, D.P., Morisette, J.T., 2002. An overview of MODIS Land data processing and product status. *Remote Sens. Environ.* 83 (1–2), 3–15.

Kalnay, E., Cai, M., 2003. Impact of urbanization and land-use change on climate. *Nature* 423 (6939), 528, 528.

Krayenhoff, E.S., Moustauoui, M., Broadbent, A.M., Gupta, V., Georgescu, M., 2018. Diurnal interaction between urban expansion, climate change and adaptation in US cities. *Nat. Clim. Change* 8, 1097(–+).

Li, M.M., Song, Y., Huang, X., Li, J.F., Mao, Y., Zhu, T., Cai, X.H., Liu, B., 2014. Improving mesoscale modeling using satellite-derived land surface parameters in the Pearl River Delta region, China. *J. Geophys. Res. Atmos.* 119, 6325–6346.

Li, M.M., Wang, T.J., Xie, M., Zhuang, B.L., Li, S., Han, Y., Song, Y., Cheng, N.L., 2017. Improved meteorology and ozone air quality simulations using MODIS land surface parameters in the Yangtze River Delta urban cluster, China. *J. Geophys. Res. Atmos.* 122, 3116–3140.

Liao, W., Wang, D., Liu, X., Wang, G., Zhang, J., 2017. Estimated influence of urbanization on surface warming in Eastern China using time-varying land use data. *Int. J. Climatol.* 37, 3197–3208.

Loveland, T.R., Reed, B.C., Brown, J.F., Ohlen, D.O., Zhu, Z., Yang, L., Merchant, J.W., 2000. Development of a global land cover characteristics database and IGBP DISCover from 1 km AVHRR data. *Int. J. Rem. Sens.* 21, 1303–1330.

Morrison, H., Pinto, J.O., Curry, J.A., McFarquhar, G.M., 2008. Sensitivity of modeled arctic mixed-phase stratocumulus to cloud condensation and ice nuclei over regionally varying surface conditions. *J. Geophys. Res. Atmos.* 113 (D5).

Oke, T.R., 1982. The energetic basis of the urban heat island. *Q. J. R. Meteorol. Soc.* 108 (455), 1–24.

Parry, M., Parry, M.L., Canziani, O., Palutikof, J., Van der Linden, P., Hanson, C., 2007. *Climate Change 2007-impacts, Adaptation and Vulnerability*. In: Working Group II Contribution to the Fourth Assessment Report of the IPCC, vol. 4. Cambridge University Press.

Peng, S.S., Piao, S.L., Ciaia, P., Friedlingstein, P., Ottle, C., Breon, F.M., Nan, H.J., Zhou, L.M., Myneni, R.B., 2012. Surface urban heat island across 419 global big cities. *Environ. Sci. Technol.* 46, 696–703.

Peng, S., Piao, S., Zeng, Z., Ciaia, P., Zhou, L., Li, X., Myneni, R., Yin, Y., Zeng, H., 2014. Afforestation in China cools local land surface temperature. *Proc. Natl. Acad. Sci. U. S. A.* 111, 2915–2919.

Purevdorj, T., Tateishi, R., Ishiyama, T., Honda, Y., 1998. Relationships between percent vegetation cover and vegetation indices. *Int. J. Rem. Sens.* 19, 3519–3535.

- Qian, Y., Chakraborty, T.C., Li, J., Li, D., He, C., Sarangi, C., Chen, F., Yang, X.C., Ruby Leung, L., 2022. Urbanization impact on regional climate and extreme weather: current understanding, uncertainties, and future research directions. *Adv. Atmos. Sci.* 1–42.
- Ran, L.M., Pleim, J., Gilliam, R., Binkowski, F.S., Hogrefe, C., Band, L., 2016. Improved meteorology from an updated WRF/CMAQ modeling system with MODIS vegetation and albedo. *J. Geophys. Res. Atmos.* 121, 2393–2415.
- Rodell, M., Houser, P.R., Jambor, U., Gottschalck, J., Mitchell, K., Meng, C.J., Arsenault, K., Cosgrove, B., Radakovich, J., Bosilovich, M., Entin, J.K., Walker, J.P., Lohmann, D., Toll, D., 2004. The global land data assimilation system. *Bull. Am. Meteorol. Soc.* 85, 381.
- Shanghai Bureau of Statistics, 2017. Shanghai Statistical Yearbook. China Statistics Press, Beijing, China.
- Shen, P., Zhao, S., Ma, Y., 2021. Perturbation of urbanization to earth's surface energy balance. *J. Geophys. Res. Atmos.* 126, 8.
- Sun, L.Q., Chen, J., Li, Q.L., Huang, D., 2020. Dramatic uneven urbanization of large cities throughout the world in recent decades. *Nat. Commun.* 11.
- Sun, Y., Zhang, X.B., Ren, G.Y., Zwiers, F.W., Hu, T., 2016. Contribution of urbanization to warming in China. *Nat. Clim. Change* 6, 706–710.
- Wan, Z.M., 2014. New refinements and validation of the collection-6 MODIS land-surface temperature/emissivity product. *Remote Sens. Environ.* 140, 36–45.
- Wang, X., Guo, W., Qiu, B., Liu, Y., Sun, J., Ding, A., 2017. Quantifying the contribution of land use change to surface temperature in the lower reaches of the Yangtze River. *Atmos. Chem. Phys.* 17, 4989–4996.
- Wang, W., Shu, J., 2020. Urban renewal can mitigate urban heat islands. *Geophys. Res. Lett.* 47, e2019GL085948.
- Yang, X., Hou, Y., Chen, B., 2011. Observed surface warming induced by urbanization in east China. *J. Geophys. Res. Atmos.* 116.
- Yang, B., Yang, X., Leung, L.R., Zhong, S., Qian, Y., Zhao, C., Chen, F., Zhang, Y., Qi, J., 2019. Modeling the impacts of urbanization on summer thermal comfort: the role of urban land use and anthropogenic heat. *J. Geophys. Res. Atmos.* 124, 6681–6697.
- Zhao, L., Lee, X., Smith, R.B., Oleson, K., 2014. Strong contributions of local background climate to urban heat islands. *Nature* 511 (7508), 216–219.
- Zhao, G.S., Dong, J.W., Cui, Y.P., Liu, J.Y., Zhai, J., He, T., Zhou, Y.Y., Xiao, X.M., 2019. Evapotranspiration-dominated biogeophysical warming effect of urbanization in the Beijing-Tianjin-Hebei region, China. *Clim. Dynam.* 52, 1231–1245.
- Zhao, S., Liu, S., Zhou, D., 2016. Prevalent vegetation growth enhancement in urban environment. *Proc. Natl. Acad. Sci. U. S. A* 113 (22), 6313–6318.
- Zhang, X., Tang, Q., Zheng, J., Ge, Q., 2013. Warming/cooling effects of cropland greenness changes during 1982–2006 in the North China Plain. *Environ. Res. Lett.* 8 (2), 024038.
- Zhang, Q., Zheng, Y.J., Singh, V.P., Luo, M., Xie, Z.H., 2017. Summer extreme precipitation in eastern China: mechanisms and impacts. *J. Geophys. Res. Atmos.* 122 (5), 2766–2778.
- Zhang, Z., Wang, K., 2021. Quantifying and Adjusting the Impact of Urbanization on the Observed Surface Wind Speed over China from 1985 to 2017. *Fundamental Research*, pp. 785–791.
- Zhou, D., Zhao, S., Liu, S., Zhang, L., Zhu, C., 2014. Surface urban heat island in China's 32 major cities: spatial patterns and drivers. *Remote Sens. Environ.* 152, 51–61.
- Zhou, L.M., Dickinson, R.E., Tian, Y., Fang, J., Li, Q.X., Kaufmann, R.K., Tucker, C., Myneni, R.B., 2004. Evidence for a significant urbanization effect on climate in China. *Proc. Natl. Acad. Sci. U. S. A* 101, 9540–9544.